© 2015. Published by The Company of Biologists Ltd | The Journal of Experimental Biology (2015) 218, 480-490 doi:10.1242/jeb.104141

RESEARCH ARTICLE

Pigeons produce aerodynamic torques through changes in wing trajectory during low speed aerial turns

Ivo G. Ros[1,*], Marc A. Badger[2], Alyssa N. Pierson[3], Lori C. Bassman[3] and Andrew A. Biewener[1]

ABSTRACT

The complexity of low speed maneuvering flight is apparent from the combination of two critical aspects of this behavior: high power and precise control. To understand how such control is achieved, we examined the underlying kinematics and resulting aerodynamic mechanisms of low speed turning flight in the pigeon (*Columba livia*). Three birds were trained to perform 90 deg level turns in a stereotypical fashion and detailed three-dimensional (3D) kinematics were recorded at high speeds. Applying the angular momentum principle, we used mechanical modeling based on time-varying 3D inertia properties of individual sections of the pigeon's body to separate angular accelerations of the torso based on aerodynamics from those based on inertial effects. Directly measured angular accelerations of the torso were predicted by aerodynamic torques, justifying inferences of aerodynamic torque generation based on inside wing versus outside wing kinematics. Surprisingly, contralateral asymmetries in wing speed did not appear to underlie the 90 deg aerial turns, nor did contralateral differences in wing area, angle of attack, wingbeat amplitude or timing. Instead, torso angular accelerations into the turn were associated with the outside wing sweeping more anteriorly compared with a more laterally directed inside wing. In addition to moving through a relatively more retracted path, the inside wing was also more strongly pronated about its long axis compared with the outside wing, offsetting any difference in aerodynamic angle of attack that might arise from the observed asymmetry in wing trajectories. Therefore, to generate roll and pitch torques into the turn, pigeons simply reorient their wing trajectories toward the desired flight direction. As a result, by acting above the center of mass, the net aerodynamic force produced by the wings is directed inward, generating the necessary torques for turning.

KEY WORDS: *Columba livia*, Turning, Aerodynamics, Dynamics modeling, Inertia

INTRODUCTION

To gain insight into the control of flight maneuvers, an understanding of the mechanics and aerodynamics involved in turning is needed. However, to date, turning flight has received little attention compared with steady forward flight. Mechanistically, the task of turning consists of two conceptually separate components: (1) re-direction of the animal's flight path and (2) reorientation of the animal's body.

Re-direction of the flight path (involving changes in translational movement) requires centripetal force production. Slowly flying vertebrates, including horseshoe bats, pigeons, fruit bats and cockatoos, all bank to orient the net aerodynamic force into the turn, analogous to how fixed-wing aircraft turn (Aldridge, 1986; Warrick, 1998; Hedrick and Biewener, 2007; Iriarte-Díaz and Swartz, 2008; Ros et al., 2011).

Reorientation of the torso (involving rotational movement) in flight can be achieved using two physical principles: (i) aerodynamic forces that induce torques about the center of mass (CM), and (ii) inertia-based changes in angular momentum of body segments that result in net changes in body orientation (Frohlich, 1980; Hedrick et al., 2007). Three-dimensional (3D) analysis of the mass distributions and time-varying configurations of the head, torso and wings can be used to determine both aerodynamics- and inertia-based maneuvering in flying birds.

Irrespective of the nature of the torque-generating mechanisms, the initiation and active control of maneuvering flight requires asymmetries in force production by the animal's locomotor system. Thus, in order to identify the underlying neuromuscular control mechanisms of turning flight, such mechanisms must be resolved on a fine time scale (within wingbeats).

Prior work has shown that pigeons and cockatoos redirect net aerodynamic forces through bilateral asymmetries in both downstroke velocity and angular momentum of the two wings (Warrick and Dial, 1998; Hedrick et al., 2007). Furthermore, pigeons maneuvering through a course with multiple turns generate small, sequential, pectoralis muscle force asymmetries to bank and navigate through the course (Warrick et al., 1998).

Recently, we (Ros et al., 2011) have shown that reorientations of the pigeon's torso are integral to low speed turning flight. Furthermore, torso rotations underlying flight path changes (constituting torque generation for steering) were found to occur subsequent to readily observable head rotations (head saccades) during the downstroke of the same wingbeat cycle (I.G.R. and A.A.B., in review). These torso rotations must be produced by torques resulting from asymmetrical force production by the wings and/or tail. Here, we sought to identify the key mechanism underlying low speed turning in pigeons, by testing whether the relevant turning torques are of an aerodynamic or inertial nature, and by investigating how contralateral wing movement asymmetries underlie torque generation. Because wingbeats containing head saccades early in the turn likely display the strongest torque generation (I.G.R. and A.A.B., in review), 18 specific wingbeats were selected for analysis (see Materials and methods for details). Based on previous findings in pigeons, cockatoos and bats (Warrick and Dial, 1998; Hedrick et al., 2007; Iriarte-Díaz et al., 2011), we expected inertial and aerodynamic effects to act synergistically in rotating the torso, because both aerodynamics-based and inertia-based torques would act in the opposite direction of a faster moving wing. We hypothesized further a greater influence of aerodynamic

[1]Harvard University, Department of Organismic and Evolutionary Biology, Concord Field Station, 100 Old Causeway Road, Bedford, MA 01730, USA. [2]University of California, Berkeley, Department of Integrative Biology, 3060 VLSB #3140, Berkeley, CA 94720, USA. [3]Harvey Mudd College, Department of Engineering, 301 Platt Boulevard, Claremont, CA 91711, USA.

*Author for correspondence (ivo.ros@gmail.com)

Received 18 February 2014; Accepted 19 November 2014

The Journal of Experimental Biology

The Journal of Experimental Biology (2015) doi:10.1242/jeb.104141

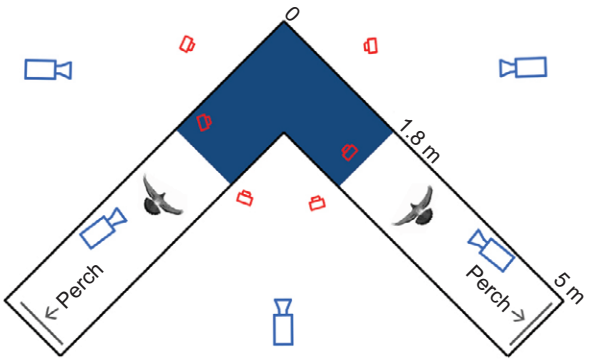

Fig. 1. Schematic top view of the flight corridor. Camera outlines represent viewing angles, with camera distances under-represented by 50%, for the high-speed (blue) and infrared-based auto-tracking (red) systems. The spatially calibrated section of the 90 deg turn (dark blue), pigeon silhouettes and perches (gray lines) are drawn to scale. Dimensions are noted along the outside of one leg of the symmetrical corridor.

torques, generated through contralateral asymmetries in wing velocity and aerodynamic angle of attack (Warrick and Dial, 1998; Hedrick et al., 2007).

To test these hypotheses, we recorded detailed kinematics of three pigeons (*Columba livia* Gmelin 1789) negotiating a level 90 deg turn (Fig. 1). By merging morphological mass-distribution measurements of the pigeon's wings, head, torso and tail with these positional data (Fig. 2), we generated a full 3D dynamics model, which can separate aerodynamics-based from inertia-based angular accelerations of the turning pigeon's torso based on application of the conservation of angular momentum principle. A determination of the timing and magnitude of both aerodynamics- and inertia-based torso angular accelerations is expected to provide a more accurate description of the rotational component of the maneuver, as well as to allow for more a detailed identification of the wing and tail kinematics underlying these torso angular accelerations.

RESULTS

The three pigeons negotiated the 90 deg level turns at a CM speed of 3.3±0.2 m s^{-1} and a wingbeat frequency of 8.3±0.3 Hz. In terms of mass distribution, each wing (distal to the shoulder) comprised 6.3±0.7% and the head 3.9±0.3% of the bird's body mass (319±33 g; Table 1) (see also van den Berg and Rayner, 1995).

Torso reorientations about all three anatomical axes

The low-speed, level turns were predominantly driven by roll and yaw rotations of the pigeons (Fig. 3). Only pitch fluctuated with consistent periodicity within the wingbeat cycle. Torso orientations about all three anatomical axes fluctuated within wingbeats, independent of changes in torso orientation across wingbeats. These latter net wingbeat reorientations about the roll and yaw torso axes, summed throughout the turn, comprised the majority of the torso reorientations across wingbeats (Table 2). The birds consistently yawed into the turn, whereas roll was initially directed into the turn and later directed outward from the turn. Net wingbeat pitch reorientations were generally directed upward (head-up).

Torque generation is based on aerodynamics

The angular momentum principle (Pratab and Ruina, 2009; Mitiguy, 2014) allowed for calculation of inertia-based angular accelerations of the torso and, indirectly, for calculation of the aerodynamics-based equivalent. Using wing-segment masses and moments of

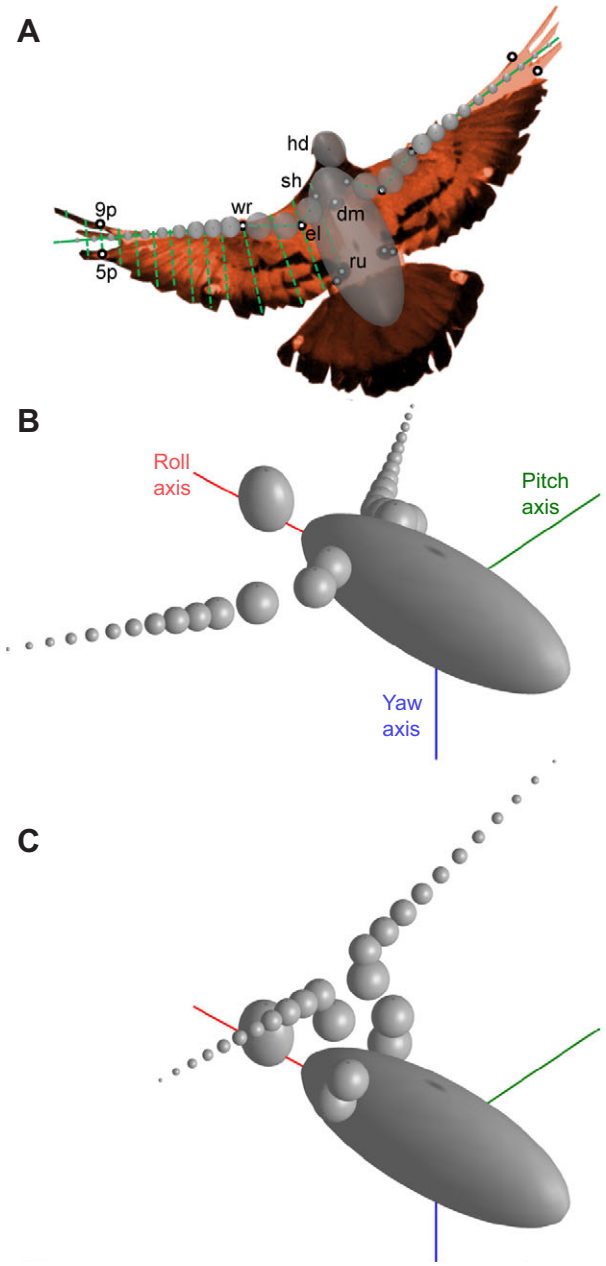

Fig. 2. Dynamics model of a pigeon based on marker locations. (A) Cut-out of a pigeon at mid-downstroke, copper-colored for contrast, with marker locations (black circles with white centers). The torso and head (hd; large and small gray ellipsoids) were treated as rigid objects for which the moments of inertia were assigned about the principal torso axes shown in B: anterio-posterior (AP; roll, red line), medio-lateral (ML; pitch, green line) and dorso-ventral (DV; yaw, blue line) axes. The torso ellipsoid, which includes the tail, is positioned based on the dorsal (dm) and rump (ru) markers. Per wing, three articulating segments (solid green lines) are represented by point masses: the brachium (one mass), antebrachium (two masses) and the hand wing distal to the wrist (11 masses). Respectively, these segments are reconstructed based on the shoulder (sh)–elbow (el), elbow–wrist (wr) and wrist–center between the ninth (9p) and fifth (5p) primary markers. Each point mass represents a wing strip (in between the dashed green lines). The volumes of the spheres and ellipsoids represent relative masses. B and C show the dynamics model of a pigeon in late downstroke (B) and near mid-upstroke (C).

inertia for the torso (which includes the tail) and head, the angular momentum principle was applied to the time-varying 3D marker positions. In brief, two separate main modeling steps were

The Journal of Experimental Biology (2015) doi:10.1242/jeb.104141

Table 1. Morphological inertia properties measured for *Columba livia*: segment masses

Segment	% Body mass
Torso (including tail)	83.6±1.3
Head	3.9±0.3
Brachium	1.5±0.3
Ante-brachium	2.9±0.4
Hand wing	1.9±0.1

Data are means ± s.d. (*N*=3).

Table 2. Net wingbeat reorientations accumulated throughout the turn

Torso rotation components	Reorientation (deg)
Roll	76.8±13.6
Pitch	42.6±1.6
Yaw	58.1±4.3

Data are means ± s.d. (*N*=3).

performed: (i) aerodynamics-based torques were estimated directly from the 3D positional data and morphological mass distributions; (ii) inertia-based torso angular acceleration were estimated based on the hypothetical case where the aerodynamic forces were assumed to be absent. The central angular momentum, i.e. the combined angular momentum of the entire body about the collective CM, can be calculated from time-varying mass distribution data (see Eqn 1). The aerodynamic torque follows directly from the rate change of the central angular momentum, whereas, by hypothetically equating the aerodynamic torque to zero, the inertial angular effect of measured wing motions on the pigeon's torso can be inferred (see Materials and methods for details).

We found that aerodynamic torques, and not inertia-based angular momentum exchanges between the wings and the rest of the bird (torso, head and tail), predicted observed torso angular roll and pitch accelerations (Fig. 4). Estimated angular accelerations of the torso based on aerodynamics correlated positively with measured accelerations about each of the principal torso axes. These aerodynamics-based estimates most reliably predicted pitch rotations ($P<0.01$, $R^2=0.89$), with significant torso acceleration correlations about both roll ($P<0.01$, $R^2=0.72$) and yaw ($P<0.01$, $R^2=0.62$) of similar strength. The range of estimated yaw accelerations was smallest, and yaw was the only axis about which inertia-based estimates also predicted observed torso accelerations ($P<0.01$, $R^2=0.41$; Fig. 4). During the turning wingbeats selected for analysis of torque-generating mechanisms, roll rotations were initiated early and arrested late in the downstroke, with a peak in angular velocity directed into the turn at mid-downstroke (Fig. 5). Variable roll velocities were of much smaller magnitude during the upstroke. Torso pitch velocities and accelerations consistently varied with wingbeat phase: head-up (positive) pitch acceleration peaked near the middle of upstroke and approximately two-thirds into downstroke, coincident with negative roll acceleration (out of the turn), whereas head-down (negative) pitch acceleration peaked near the first third of downstroke, coincident with the peak in positive roll acceleration. These pitch patterns were consistent for all wingbeats analyzed throughout the turn, and consistent with aerodynamic torques (Fig. 8A,B). In contrast, torso roll and yaw aerodynamic torques and resulting angular movements (not shown) were more variable throughout the turn. Yaw velocity was consistently positive (directed into the turn) over the full wingbeat cycle (Fig. 5A), with a moderate deceleration phase near the end of downstroke (Fig. 5B).

Model sensitivity and data validation

Approaches containing double derivatives of positional data are sensitive to measuring errors, warranting sensitivity tests of our dynamics model. Artificially varying the wing length by ±10% and changing the mass of the hand wings (the point masses distal to the wrist) by ±10% of the wing mass did not change statistical trends between inertia- or aerodynamics-based and observed angular torso accelerations. Artificially increasing the wing lengths or hand wing masses resulted in a slightly reduced regression model fit between aerodynamics-based estimates and observed torso angular accelerations [R^2 values for roll (0.72), pitch (0.89) and yaw (0.62) decreased to 0.69, 0.87 and 0.56 for wing lengths, and decreased to or stayed equal at 0.64, 0.89 and 0.38 for hand wing masses, respectively]. Artificially decreasing wing lengths or hand wing masses led to similar changes, but in the opposite direction. The sensitivity tests most strongly affected torso acceleration estimates about the yaw axis, about which inertia-based estimates also predicted observed torso angular accelerations, albeit with a lower slope (0.34 versus 0.66) and regression model fit (R^2=0.41 versus 0.62) than aerodynamics-based estimates. Additionally, the marker-based torso angular accelerations compared well with measurements obtained from a back-mounted inertial measurement unit (IMU) in pigeons maneuvering at similar strengths and flight speeds (H. Lin, I.G.R. and A.A.B., in preparation). Besides similarities in trace shape within wingbeat cycles, peak torso angular velocities and accelerations reached ~900 deg s^{-1} and 7×10^4 deg s^{-2}, respectively, for both kinematics-derived and IMU-based values. Although the

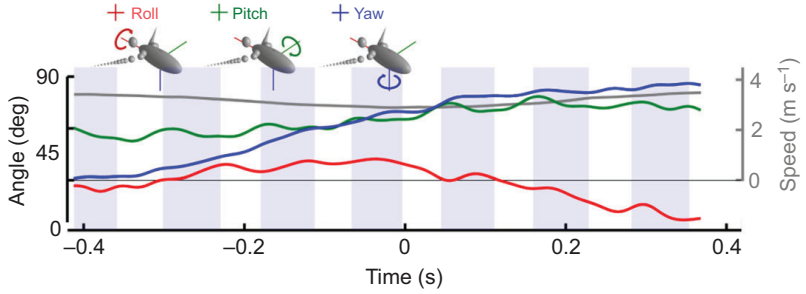

Fig. 3. Low-speed, level turns in pigeons are predominantly based on roll and yaw rotations. Integrated angular velocities about the principal torso axes throughout a representative right turn, with positive roll and yaw into the turn, as well as head-up pitch (small depictions above the figure). Initial angles are based on the inclinations of the corresponding torso axes with respect to the horizontal at the start of recording. The majority of torso reorientations occur about the roll and yaw axes. Only pitch varies periodically with the wingbeat (blue shading represents downstroke phases). Flight speed (gray trace), a one-wingbeat running average, remains approximately constant with a moderate slow down near the midpoint of the turn (*t*=0 s).

The Journal of Experimental Biology (2015) doi:10.1242/jeb.104141

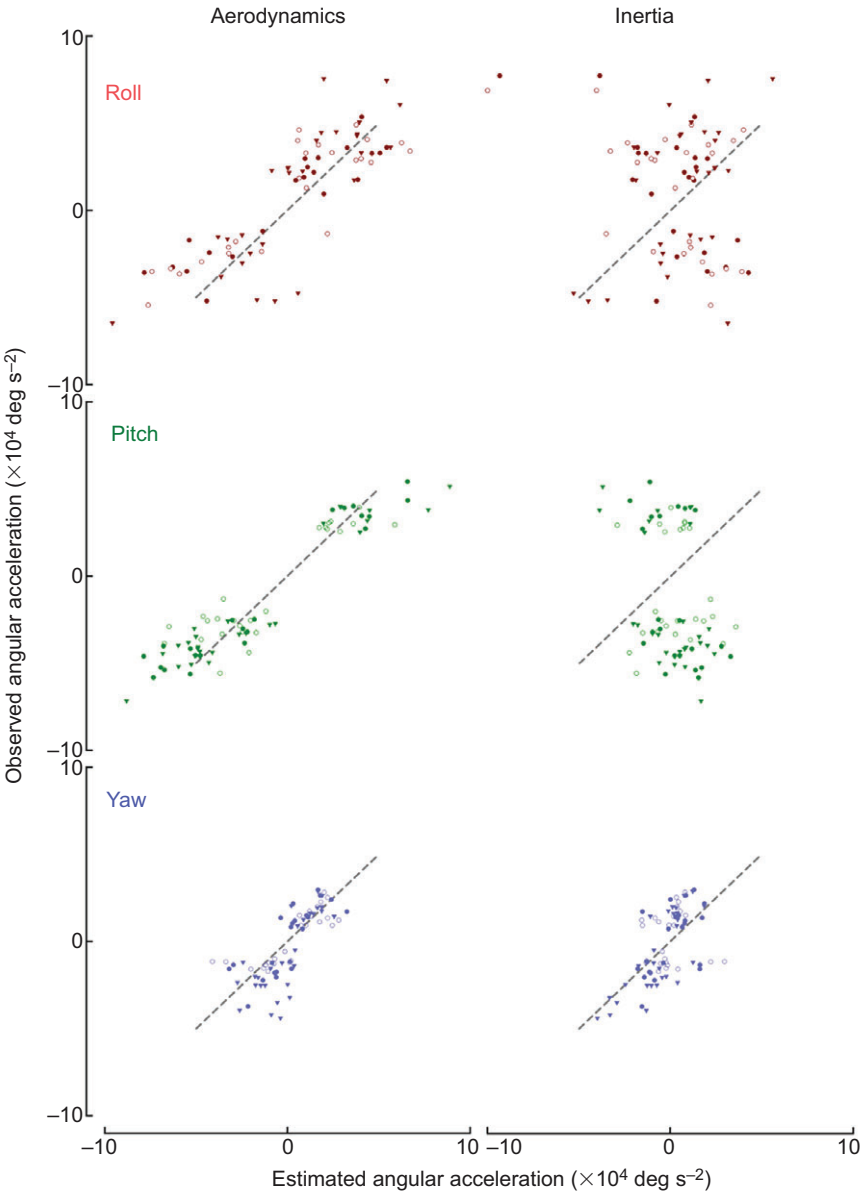

Fig. 4. Aerodynamic estimates predict torso angular accelerations. Torso angular accelerations based on aerodynamic torque estimates ('Aerodynamics'; left panels) predict measured torso accelerations throughout two left and two right turns per individual (N=3; plotted symbols), about roll (red; R^2=0.72, P<0.01), pitch (green; R^2=0.89, P<0.01) and yaw (blue; R^2=0.62, P<0.01) axes. Torso angular accelerations based on rate of momentum exchange ('Inertia'; right panels) between the wings and the torso do not correlate with observed roll and pitch torso accelerations, but do correlate with observed yaw accelerations (blue; R^2=0.41, P<0.01). The regression analyses about the principal torso axes are based on one (peak) torso acceleration per wingbeat and corrected for trial and wingbeat numbers and individual effects.

IMU recordings were of pigeons during different maneuvers and should not be directly compared, their similar patterns are affirmative and support the sensitivity tests in illustrating the robustness of our finding of aerodynamics-based torque generation.

Torque-generating mechanisms

Turning wingbeats selected for analysis of torque-generating mechanisms were characterized by differentially swept wing trajectories, or paths of wing motion relative to the torso (Fig. 6), accompanied by contralateral differences in hand wing axial orientation (pronation–supination) (Fig. 7A). Corresponding with the peak in roll acceleration observed early in downstroke (Fig. 5B), the outside wing was initially positioned and swept more anteriorly compared with a more laterally directed inside wing trajectory (Fig. 6). In concert with the contralateral asymmetry in wing trajectories, the inside wing was more strongly pronated, or rotated forward (leading-edge down) about the wing's long axis during the first half of the downstroke (Fig. 7A). This contralateral difference in pronation was reversed in the second half of the downstroke, through supination of the inside wing and pronation of the outside wing near the middle of the downstroke (Fig. 7A). As the pigeon's torso rolled into the turn in the downstroke (Fig. 5A), the inside wing also acquired a higher speed (Fig. 7B) and became oriented more laterally (Fig. 7C) compared with the outside wing.

DISCUSSION

Aerodynamics- and inertia-based angular accelerations of pigeons' torsos during low speed turning flight were determined using segment masses, time-varying 3D inertia properties and torso and wing configurations. Using this approach, we have shown that measured torso angular accelerations correlate strongly with observed aerodynamic torques, justifying a comparison of inside wing versus outside wing kinematic proxies for aerodynamic torque-generating mechanisms. In comparison to previous findings (Warrick and Dial, 1998), contralateral asymmetries in wing speed do not appear to underlie the aerial turns we analyzed, and, surprisingly, nor do contralateral differences in wing area, angle of attack, wingbeat amplitude or timing (supplementary material

The Journal of Experimental Biology (2015) doi:10.1242/jeb.104141

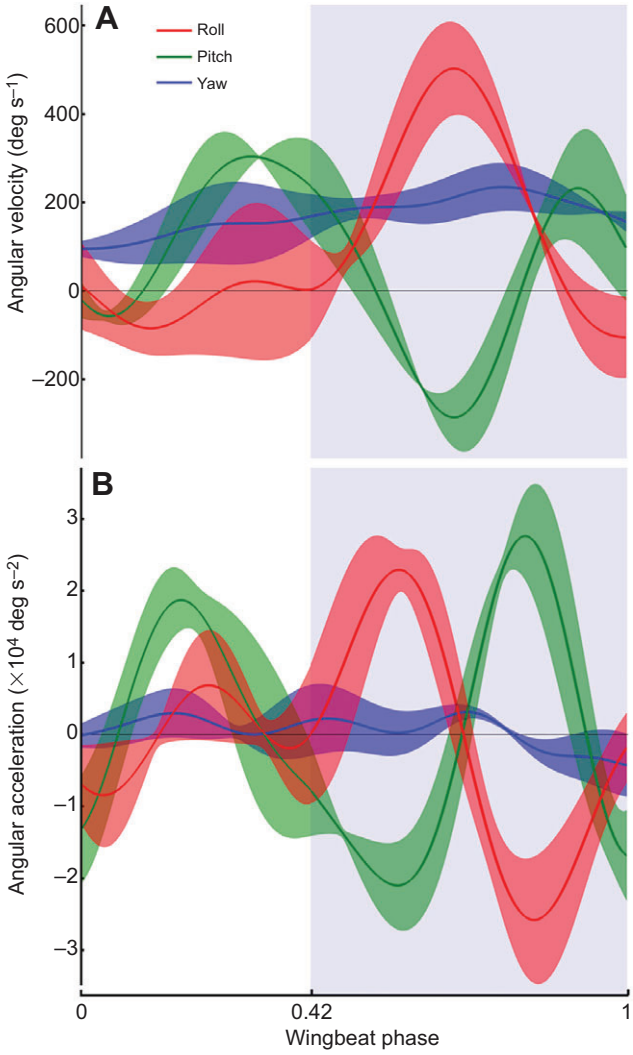

Fig. 5. Roll velocity is initiated early and arrested late in the downstroke. (A) Mean ± s.d. of individual mean (*N*=3) torso velocities in roll (red), pitch (green) and yaw (blue) throughout three left and three right selected wingbeats early in the turn, and normalized to the wingbeat period. Near the middle of the downstroke (blue shading), the torso pitches bill-down (–) and rolls into the turn (+). (B) The mean individual roll and pitch accelerations peak in the first half of the downstroke, with extremes reversed in the second half of the downstroke, arresting the roll velocity and reversing the pitch velocity, respectively, in A. Pitch accelerations also show peaks near mid-upstroke, whereas roll accelerations are more variable during the upstroke.

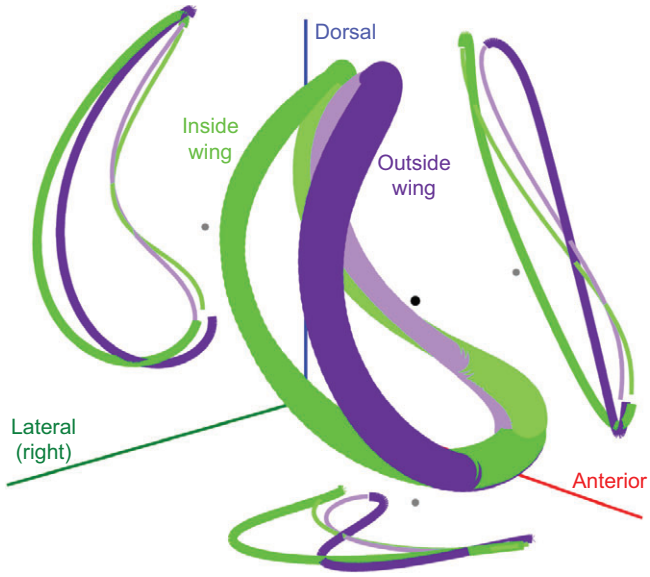

Fig. 6. Turning wingbeats are characterized by differentially swept wing trajectories. Mean ± s.d. (trace thickness) of individual mean trajectories of the distal wing marker for the inside (green) and outside (purple) wing for the same selected turning wingbeats as in Fig. 5. Both trajectories are represented as a right wing, by mirroring the left wing in the mid-sagittal plane. The trajectories are displayed relative to the torso frame, represented by the anterior (red), right (green) and dorsal (blue) directions, as well as the right shoulder location (black circle). The means of the 3D trajectories, with the upstroke in a lighter shade, are projected on each of the anatomical planes, emphasizing the more protracted (anteriorly projected) path of the outside wing early in the downstroke.

Fig. S1). Instead, to generate roll and pitch torques into the turn, the pigeons reorient their wing trajectories toward the desired direction while rotating their hand-wings such that similar aerodynamic angles of attack are maintained between the inside and outside wing (Figs 6 and 7). As a result, the aerodynamic force is directed into the turn and, by acting above the center of mass, generates the necessary turning torques (Fig. 8).

Our results show that pigeons use a complex combination of roll, pitch and yaw torso rotations to make level turns, with the largest contribution resulting from reorientations about the antero-posterior axis of the torso (Fig. 2, Table 2). These roll rotations serve to redirect the net aerodynamic force, producing changes in flight path (Ros et al., 2011): during the first half of the turn, pigeons roll into the turn, whereas during the second half they roll out. The observed roll patterns may also enable changes in torso pitch to contribute to the turn. Because of the bird's banked orientation while turning (Warrick, 1998; Hedrick and Biewener, 2007; Ros et al., 2011), head-up pitch reorientations can contribute to reorienting the bird's body into the desired direction. However, neither the summed net wingbeat yaw nor pitch reorientations fully matched the 90 deg of the turn (Table 2), illustrating the need for a composite of whole-body rotation components to simultaneously meet the translational (flight path changes and gravitational support) and rotational (acquisition of the desired new flight orientation) requirements of the turn.

The consistent patterns of aerodynamics-based pitch acceleration and torque observed relative to wingbeat phase (Fig. 3, Fig. 5B, Fig. 8A,B), in combination with wing positioning throughout the wingbeat cycle, strongly suggest that the center of pressure of the resultant aerodynamic force is positioned dorsal to the bird's CM during the first half of downstroke, and ventral and anterior to the CM near the second half of downstroke, through the middle of upstroke. These inferences agree with previous findings that aerodynamic forces act dorsal to the center of mass during the downstroke of the Japanese white-eye (Su et al., 2011) and corroborate the active aerodynamics of the pigeon's tip-reversal upstroke (Crandell and Tobalske, 2011; Ros et al., 2011).

Contralateral differences in wing trajectory and hand wing pronation (Fig. 6, Fig. 7A) coincide with roll accelerations observed early in the downstroke that are directed towards the inside wing (Fig. 5B). Consequently, these kinematic asymmetries of the wings likely indicate the aerodynamic mechanism used to generate the necessary steering torque. Torso accelerations that increase the central angular momentum of the bird require

The Journal of Experimental Biology

The Journal of Experimental Biology (2015) doi:10.1242/jeb.104141

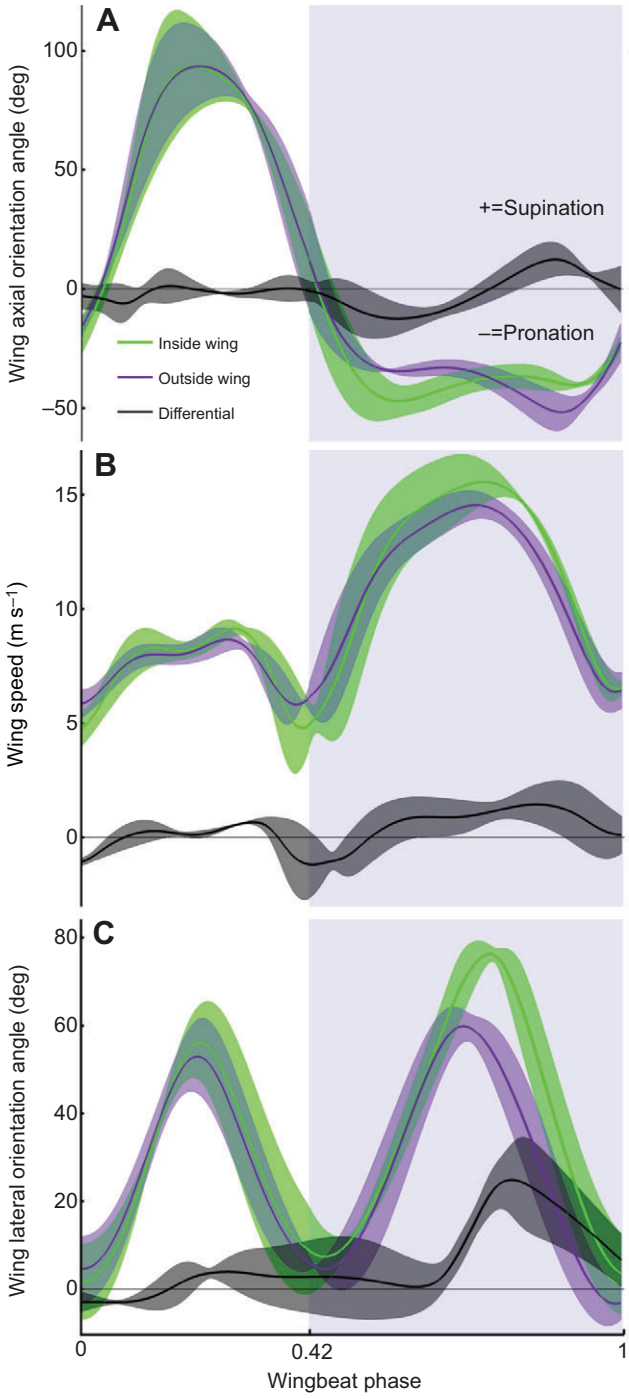

Fig. 7. Wing pronation accompanies a more caudally swept inside wing, whereas a greater wing speed and later projection aerodynamically dampen roll velocity. (A) For the same wingbeats as in Figs 5 and 6, during the upstroke, the inside wing (green) and outside wing (purple) supinate and subsequently pronate about the wing long-axis in synchrony. Early in the downstroke, the inside wing pronates to a larger degree than the outside wing, resulting in an inside versus outside wing differential that is negative, or pronated (black trace ± s.d.). The more pronated inside wing in combination with the contralateral difference in wing trajectory maintains comparable angles of attack between the wings. However, these wing-configuration and kinematic differences likely result in aerodynamic forces that act above the center of mass to be directed upwards and to the right side of the torso, causing the pitch down and roll torques into the turn. (B) Inside wing speed (of the ninth primary marker) starts surpassing outside wing speed as the roll velocity (A) increases towards the inside wing. The higher speed of the inside wing persists longer than the roll velocity, indicating its contribution to passive aerodynamic roll damping, aided by a more lateral orientation angle (C) of the inside wing (the angle between the wing long axis and the sagittal plane of the torso).

differential activation of contralateral flight muscles. Compared with previous findings (Warrick and Dial, 1998), we find here that these ‘active’ torso angular accelerations do not correlate with contralateral asymmetries in wing speed relative to the torso (relevant from a control perspective) or in the inertial frame (relevant to aerodynamics). Nor were contralateral differences in wing length (which may serve as a proxy for wing area), aerodynamic angle of attack, wingbeat amplitude or timing found to correlate with observed patterns of torso angular acceleration. Instead, pigeons appear to reorient the flapping sweep of their wing trajectories toward the desired direction, while preventing aerodynamic angle of attack asymmetries through hand wing rotations. These differences in wing trajectories between the inside and outside wing likely redirect the net aerodynamic force into the turn (Fig. 8D). Assuming that this aerodynamic force acts dorsal to the bird’s CM, the redirected aerodynamic force would generate the observed roll towards the inside wing, in addition to producing head-down pitch (Fig. 8C,D).

Given broad similarities in the avian body plan and the fairly simple nature of the aerodynamic torque-generating mechanism described here, we believe it is likely that other bird species use the same mechanism to generate aerodynamic torques during slow turning flight. For example, cockatoos turning at low speeds displayed contralateral differences in wing kinematics similar to those described here, even though these kinematic differences in the cockatoos did not relate significantly to roll accelerations (Hedrick and Biewener, 2007). It is likely that this reflects the greater kinematic resolution of the current study and recognition that redirection of aerodynamic force occurs at key points of turning that follow head saccades (I.G.R. and A.A.B., in review). Asymmetries in wing trajectory and pronation were also found previously in pigeons (Warrick and Dial, 1998). However, technical limitations prevented measurements of pronation angles throughout wingbeat cycles and, thus, linking these asymmetries to torque generation. In the current study, the 18 turning wingbeats selected for analysis generally occurred early in the turn where the strongest trajectory changes occur (Ros et al., 2011), although the described torque-generating mechanism can be expected to be used throughout turns when trajectory changes are needed.

The observed contralateral differences in wing trajectory and hand wing pronation further corroborate the idea that antebrachial musculature is involved in low speed flight maneuvers (Bilo et al., 1985; Bilo, 1994; Dial, 1992). Our results, however, do not exclude the potential role of differential force production between contralateral pectoralis muscles of the inside and outside wing (Warrick et al., 1998) or corresponding differential wing speeds (Warrick and Dial, 1998) as additional or complementary torque-generating mechanisms. It is possible that our selection of key turning wingbeats related to flight trajectory changes excluded other wingbeats in which wing speed asymmetries may contribute to torque production for turning. It is also likely that our improved resolution of temporal and spatial kinematics allow us improved accuracy for wing kinematics relative to movements of the bird’s torso. Based on our analysis, we found that differences in wing speed occur near the middle and end of the downstroke (Fig. 7B), when roll velocities are substantial and are subsequently arrested (Fig. 5A). Because rotation of the torso increases the speed of the

The Journal of Experimental Biology (2015) doi:10.1242/jeb.104141

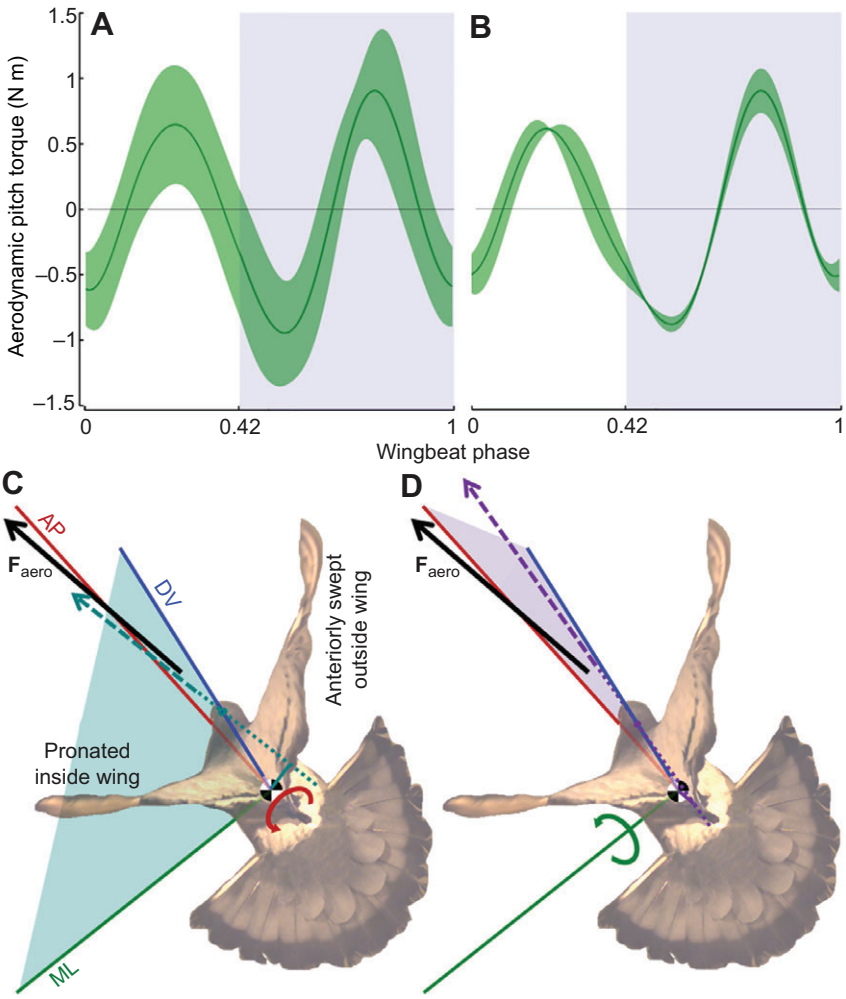

Fig. 8. Interpretation of aerodynamic pitch and roll torques. Aerodynamic pitch torques, (A) normalized to the wingbeat cycle, of a representative individual (mean ± s.d. of 20 turning wingbeats) were (B) consistent across individuals (mean ± s.d. of individual means, *N*=3). Negative (head-down) aerodynamic pitch torques early in downstroke and at the downstroke–upstroke transition are offset by positive peaks in pitch torque in the latter halves of both the upstroke and downstroke. These patterns, combined with wing stroke kinematics (Figs 6 and 7), indicate that the resultant aerodynamic force acts behind S_{CM} (black–white symbol in C and D) during the early part of the downstroke and subsequently travels antero-ventrally to produce an opposing head-up torque by acting in front of S_{CM} later in downstroke. (C,D) Interpretation of roll-in (C) and pitch-down (D) torque-generating mechanisms. Rear-view of a cut-out of a pigeon entering a left turn, early in the downstroke, with superimposed anatomical roll (AP; red), pitch (ML; green) and yaw (DV; blue) axes (see Fig. 2B). (C) An approximation of the instantaneous 3D resultant aerodynamic force (black vector, $\mathbf{F}_{aero}$) at this moment of the wingbeat cycle is projected onto the transverse ML–DV plane (teal dashed vector within the teal shading). The line of action (teal dotted line) of this transverse projection extends to the right of S_{CM}, with a moment arm (solid teal line) to produce a left roll torque into the turn (red circular arrow). A more pronated left wing and a more anteriorly swept right wing result in an aerodynamic force that is directed left of the mid-sagittal plane. (D) The 3D resultant aerodynamic force, $\mathbf{F}_{aero}$, projected on to the mid-sagittal AP–DV plane (purple dashed vector within purple shading) acts, similarly, behind S_{CM} to produce a head-down pitch torque (green circular arrow). The picture was taken of a turning pigeon without markers.

wing on the side of the bird that moves with torso roll (the inside wing), such a passive rotational damping mechanism (Hedrick et al., 2009) may help to arrest the bird's roll velocity near the end of the downstroke. By projecting more laterally during the second half of downstroke (Fig. 6, Fig. 7C), the inside wing's moment arm for aerodynamic force about the roll axis may also be increased, further enhancing rotational damping. To the extent that torso rotations are passively damped by these mechanisms, such torso rotations would mitigate the need for differential activation of contralateral wing muscles to arrest existing torso angular rotations.

Our mechanical modeling approach depends on second time derivatives of estimated mass distributions, which renders it sensitive to the propagation of measuring errors. Therefore, we limit our conclusions based on the dynamics model to correlative patterns that indicate the nature of the torques underlying these turns (inertia or aerodynamics; Fig. 4) and to consistent aerodynamic pitch torques averaged over many turning wingbeats (Fig. 8A,B) that aid in interpreting the aerodynamic torque-generating mechanism used to turn (Fig. 8C,D). More specific inferences, such as time-varying torque patterns within individual wingbeats, await further validation of the modeling and error analyses.

By examining the activation and strain patterns of flight muscles throughout aerial turns, we plan to further explore the neuromuscular components of flight control. Differential activation of distal wing muscles has been found to relate to steering in simulated flight in pigeons (Bilo and Bilo, 1983). Additionally, the extensor metacarpus radialis, an antebrachial hand wing extensor, was found to predict lower frequency components of turning (Hedrick and Biewener, 2007). Differential activation of inside versus outside wing muscles that are likely to control wing trajectory, such as the scapulohumeralis caudalis and pectoralis pars sternobrachialis (Dial et al., 1988; Baier et al., 2013), and hand wing pronation, such as the extensor metacarpi radialis and the ulnometacarpalis ventralis (Vazquez, 1995), may also play key roles in turning flight.

MATERIALS AND METHODS

Animal training and flight recording

Three rock doves (*C. livia*) were selected from 10 wild-caught individuals, based on their turning flight performance during training. These pigeons were housed, trained and studied at the Concord Field Station (Bedford, MA, USA) in accordance with protocols approved by Harvard University's Institutional Animal Care and Use Committee. The pigeons were trained to fly back and forth between two perches situated at either end of two 5 m long by 1 m wide by 2 m high netted sections, connected by a 90 deg turn (Fig. 1). The symmetrical, square-corner corridor was constructed of lightweight, 2 cm mesh nylon deer netting supported by a PVC frame consisting of 4 cm diameter piping.

Flights were recorded simultaneously using two camera systems (see Ros et al., 2011). A high-speed light video system recording at 250 Hz with 0.001 s exposure time consisted of one FastCam-X 1280 PCI, two FastCam 1024 PCI cameras (Photron USA Inc., San Diego, CA, USA) and two

RedLake PCI 500 cameras (RedLake Inc., San Diego, CA, USA). A second, infrared-based auto-tracking system recording at 240 Hz with 0.0004 s exposure time consisted of six ProReflex MCU240 cameras (Qualisys AB, Göteborg, Sweden). The two camera systems were synchronized using an electrical pulse trigger.

Marker placement and 3D positional reconstruction

Using the 11 synchronized high-speed cameras, time-varying positions of 10 mm diameter torso and tail markers as well as 4 mm diameter polystyrene wing markers were collected within a calibrated 1.8 m^3 cubic volume that encompassed the turn. Trials accepted for analysis (>90% of trials recorded) were those in which the birds (i) did not contact the netting and (ii) maintained a turning flight path relative to global horizontal of <5 deg. The markers were placed at 16 anatomical locations (see Ros et al., 2011) (Fig. 2A): dorsum at the second thoracic vertebra; left and right rump (4 cm lateral to the vertebral column over the synsacrum); center of head; left and right wing roots; left and right wrists; tip of left and right fifth primary feathers; 67% of the length of left and right ninth primary feathers; 67% along the length of left and right outer tail feathers; and left and right tip of the innermost secondary feathers. Elbow position was determined trigonometrically based on two lengths and three positions: brachial and antebrachial segment lengths and wing root, wrist, and tip of the innermost secondary feather positions. The maximum mass added to a bird by the markers, including elastic tape on the torso, was 14 g, or 4% of the body mass.

The 3D marker positions were reconstructed based on the volumetric calibration, using freely available digitization software (Hedrick, 2008). Calculations were performed in Mathematica (Wolfram Research, Champaign, IL, USA) and Matlab (MathWorks Inc., Natick, MA, USA) using custom-written scripts. Positional data were filtered with a fourth-order Butterworth filter using a low-pass cut-off frequency three times the wingbeat frequency. Cut-off frequency was determined by residual analysis (Winter, 2005). To avoid poor performance of the Butterworth filter near the tails of time series (Walker, 1998), data from 15 frames on either end of each flight trial were omitted post-filtering. The aerodynamic torque filtered with the low-pass Butterworth correlated strongly with a quintic spline (R^2=0.98).

Correlations between observed and estimated torso angular accelerations, based on one (peak) value per wingbeat, were tested with standard least squares regression models corrected for trial number, wingbeat number (relative to the geometrical center of the flight corridor) (after Hedrick et al., 2007) and individual effects (JMP, SAS Institute, Cary, NC, USA). Unless noted otherwise, results are expressed as means ± s.d.

Torso reorientations throughout the turn

Wingbeats were partitioned into upstroke and downstroke phases based on reversal of the major bending direction of the primary feathers. This reversal coincided with the instant the primary feather markers moved laterally relative to the torso, in both ventral (start of upstroke) and dorsal (start of downstroke) positions. Net wingbeat torso rotations were defined as the resulting changes in torso orientation over entire wingbeat periods and were calculated about each of the torso axes. For each of two left and two right turns per individual, at least five sequential upstroke–downstroke wingbeats were analyzed (22, 25 and 28 wingbeats for the three birds), over which net wingbeat torso rotations about each axis were accumulated over the course of the 90 deg turn (Table 2). The analyzed spatial section of the flight corridor was kept consistent across individuals, with the measured change in flight path through the turn averaging 90.0±2.1 deg across individuals.

Dynamics modeling

The angular momentum principle states that the rate of change of the angular momentum of a system, e.g. an entire bird, about its center of mass is equal to the sum of all torques (used here to mean moments of force about the mass center) on the system (Mitiguy, 2014). For the body plan of a pigeon, with many spatial degrees of freedom, the central angular momentum can be calculated through summation of the angular momentum of each body segment about the collective, or system, center of mass (S_{CM}). S_{CM} can move relative to the torso, due primarily to varying wing and head positions.

Table 3. Morphological inertia properties measured for *Columba livia*: mass moments of inertia

Segment	Roll (×10^{-5} kg m^2)	Pitch (×10^{-5} kg m^2)	Yaw (×10^{-5} kg m^2)
Torso	20.98±3.75	56.38±0.28	71.19±8.62
Head	3.90±0.45	5.93±0.90	4.42±0.13

Data are means ± s.d. (*N*=3).

To calculate the central angular momentum, a mass-distribution model was created that treated the torso/tail (modeled as one object) and head as rigid objects, and modeled each wing as a series of point masses P_i positioned along the wing segments (Fig. 2, Table 1). Here, the head was assumed to remain in a fixed orientation with respect to the torso and the mass of the tail was included in the torso, ignoring inertial effects due to independent head or tail movement relative to the torso. The wing segments were allocated based on wing anatomy (Fig. 2A). The moments of inertia about the antero-posterior (roll), medio-lateral (pitch) and dorso-ventral (yaw) axes of the head and torso (including the tail) (Table 3) were calculated from the angular swing periods during two-point suspensions (see Newman and Searle, 1957; Alexander, 1968). Additionally, the CM of the head and torso was determined by multiple single-point suspensions as the intersection of the direction of gravity. Only the wing markers were included in the morphometrics.

The angular momentum principle formulated with respect to S_{CM} states that angular momentum changes about the CM can only be achieved by external torques. Gravity produces a resultant force that acts through S_{CM} and thus does not apply a torque about S_{CM}. Aerodynamic forces are the only source of external torques about S_{CM}, and therefore the rate of change of the central angular momentum in the inertial reference frame N for the pigeon system S ($^N\mathrm{d}^N\vec{H}^{S/S_{CM}}/\mathrm{d}t$; Eqn 1) is equivalent to the aerodynamic torque acting about S_{CM}.

The expanded central angular momentum principle is given by Eqn 1 (see Appendix for derivation):

$$^N\mathrm{d}^N\bar{H}^{S/S_{CM}}/\mathrm{d}t = \sum_{i=1}^{n}\left(m^{P_i}*\left[\left(\bar{r}^{P_i/T_{CM}}-A\right)\left(D+C+B\right)\right]\right)+\left(\underline{I}^{T/T_{CM}}\cdot{}^N\bar{\alpha}^T\right)+\left(m^T*D\times A\right), \quad (1)$$

where:

$$A=\frac{1}{m^S}*\left(\sum_{i=1}^{n}\left(m^{P_i}*\bar{r}^{P_i/T_{CM}}\right)\right), \quad (2)$$

$$B={}^T\bar{a}^{P_i}+2^N\bar{\omega}^T\times{}^T\bar{v}^{P_i}, \quad (3)$$

$$C={}^N\bar{\alpha}^T\times\bar{r}^{P_i/T_{CM}}+{}^N\bar{\omega}^T\times\left({}^N\bar{\omega}^T\times\bar{r}^{P_i/T_{CM}}\right), \quad (4)$$

$$D=-\frac{1}{m^S}*\left(\sum_{i=1}^{n}\left(m^{P_i}*\left(B+C\right)\right)\right), \quad (5)$$

for which m^{P_i} is the wing point mass P_i; m^S is the mass of the system S (entire bird); $\underline{I}^{T/T_{CM}}$ is the inertia dyadic of the torso T about the center of mass of the torso; $\bar{r}^{P_i/T_{CM}}$ is the vector from the torso center of mass to P_i; ${}^T\bar{v}^{P_i}$ is the velocity of P_i in the reference frame of the torso; ${}^N\bar{\omega}^T$ is the angular velocity of the torso in the inertial frame; ${}^T\bar{a}^{P_i}$ is the acceleration of P_i in the reference frame of the torso; and ${}^N\bar{\alpha}^T$ is the angular acceleration of the torso in the inertial frame.

Even though the central angular momentum is only changed by external torques, relative movements of body segments result in the redistribution of angular momentum, which can change the orientation of the pigeon in 3D space, much like a cat righting itself in mid-air (see Frohlich, 1980). Specifically, in the absence of aerodynamic forces, the external torque about S_{CM} and, thus, the rate of change of the central angular momentum are zero. Therefore, any changes in the angular momentum of the wings will be matched by an equal and opposite change in the angular

momentum of the rest of the bird (torso, head and tail), referred to here as the torso-system. By equating the entire right-hand side of Eqn 1 to zero, the aerodynamic torque is assumed to be zero, and ${}^{N}\vec{\alpha}^{\mathrm{T}}$ can be solved for at each time step (see Appendix). By comparing the expected angular velocity from inertia-based reorientations with the measured angular velocity of the torso, torso angular accelerations based on aerodynamic forces can, in turn, be deduced. Aerodynamics-based torso angular accelerations determined this way closely matched calculated aerodynamic torques in timing and direction (not shown) and were used for further analysis, as these torso angular accelerations could be directly compared with inertia-based torso angular accelerations.

Kinematics and aerodynamic torque generation

Potential wing kinematic predictors of aerodynamic torques were assessed on an inside wing versus outside wing basis. Accordingly, inside wing kinematics were averaged, as were outside wing kinematics, for wingbeat pairs obtained from left turns and right turns. Because of the incremental yet oscillatory nature of pigeon turning flight (Warrick et al., 1998), wingbeat characteristics, such as variations in aerodynamic power output from one wingbeat to the next, could lead to higher wing speeds or angles of attack of both the inside and outside wings in a left turn compared with a right turn (or vice versa), without accurately reflecting torque-related contralateral asymmetries. The averaging of inside wing versus outside wing kinematics for wingbeat pairs recorded across left and right turn flight trials accounted for such potential differences between wingbeat cycles, as well as differential left wing–right wing marker placement.

Even though active torque generation is required to change the orientation of a flying bird, once a bird has reoriented in a particular way, say banked into a turn, even subsequent wingbeats can change the flight direction, because of the previously obtained orientation. The challenge was to identify wingbeats with active torque generation that were of similar dynamic nature and of opposite sign, so that wingbeat pairs could be analyzed on the described inside versus outside wing basis.

Previously, we found that the occurrence of head saccades indicates wingbeats that contain active torque generation that lead to reorientations of the bird related to flight path changes (I.G.R. and A.A.B., in review). In addition to the before-mentioned wingbeat-to-wingbeat differences such as aerodynamic power and handedness, wingbeats can start with existing angular momentum, further complicating the identification of wingbeats to select for the analysis of torque generation. Eighteen key turning wingbeats (three left and three right per individual) were selected from wingbeats with large head saccades, generally occurring early in the turn, based on kinematic consistency in terms of torso angular velocity and acceleration profiles (Fig. 5). The selection of these key turning wingbeats was not based on wing kinematics. Consistent but opposing angular torso kinematics do not preclude differences in aerodynamic flight power or negate handedness, still requiring an inside versus outside wing analysis of the aerodynamic torque-generating mechanism.

APPENDIX

Derivation of the angular momentum principle

The pigeon was modeled as consisting of two sub-systems: (i) a torso-system and (ii) a wing-system. The torso-system represented the torso, tail and head as a single rigid object. The mass distribution of both wings was represented by the wing-system, consisting of 14 point masses distributed along each wing (Fig. 2). The sum of all aerodynamic moments $\vec{M}^{S/S_{\mathrm{CM}}}$ on system S about the system center of mass S_{CM} was equal to the time derivative of the angular momentum ${}^{N}\vec{H}^{S/S_{\mathrm{CM}}}$ of the system about S_{CM} in the inertial frame N.

$$\vec{M}^{S/S_{\mathrm{CM}}} = \frac{{}^{N}\mathrm{d}\,{}^{N}\vec{H}^{S/S_{\mathrm{CM}}}}{\mathrm{d}t}. \tag{A1}$$

This relationship only held if moments and angular momentum were computed about S_{CM}.

We first divided ${}^{N}\vec{H}^{S/S_{\mathrm{CM}}}$ into the torso-system (${}^{N}\vec{H}^{\mathrm{T}/S_{\mathrm{CM}}}$) and wing-system ($\Sigma_{i=1}^{n}\,{}^{N}\vec{H}^{P_i/S_{\mathrm{CM}}}$) components (with P_i representing the ith point mass of the 14 point masses comprising the segments of each wing):

$${}^{N}\vec{H}^{S/S_{\mathrm{CM}}} = {}^{N}\vec{H}^{\mathrm{T}/S_{\mathrm{CM}}} + \left(\sum_{i=1}^{n} {}^{N}\vec{H}^{P_i/S_{\mathrm{CM}}}\right). \tag{A2}$$

The goal, then, was to represent:

$$\vec{M}^{S/S_{\mathrm{CM}}} = \frac{{}^{N}\mathrm{d}\,{}^{N}\vec{H}^{S/S_{\mathrm{CM}}}}{\mathrm{d}t} = \frac{{}^{N}\mathrm{d}\,{}^{N}\vec{H}^{\mathrm{T}/S_{\mathrm{CM}}}}{\mathrm{d}t} + \left(\sum_{i=1}^{n} \frac{{}^{N}\mathrm{d}\,{}^{N}\vec{H}^{P_i/S_{\mathrm{CM}}}}{\mathrm{d}t}\right), \tag{A3}$$

in terms of measured quantities by expanding the terms using equations given in Mitiguy (Mitiguy, 2008).

From the mass distribution data, we computed the following: m^{P_i} is the wing point mass P_i; m^{S} is the mass of the system S (entire bird); and $\underline{\boldsymbol{I}}^{\mathrm{T}/\mathrm{TCM}}$ is the inertia dyadic of the torso T about the center of mass of the torso. Pre- and post-multiplication of the inertia dyadic with orthogonal unit vector bases $\vec{b}_x$, $\vec{b}_y$ and $\vec{b}_z$ defining the bird reference frame gave moments and products of inertia for the corresponding bases.

From the 3D positional data, we determined the following as functions of time: $\vec{r}^{\,P_i/\mathrm{TCM}}$ is the vector from the torso center of mass to P_i; ${}^{\mathrm{T}}\vec{v}^{P_i}$ is the velocity of P_i relative to the torso (through numerical differentiation of $\vec{r}^{\,P_i/\mathrm{TCM}}$); ${}^{\mathrm{T}}\vec{a}^{P_i}$ is acceleration of P_i relative to the torso (through numerical differentiation of ${}^{\mathrm{T}}\vec{v}^{P_i}$); ${}^{N}\vec{\omega}^{\mathrm{T}}$ is the angular velocity of the torso (through numerical differentiation of positional data); and ${}^{N}\vec{\alpha}^{\mathrm{T}}$ is the angular acceleration of the torso (through numerical differentiation of ${}^{N}\vec{\omega}^{\mathrm{T}}$).

Note that the above vectors were either always represented in the bird reference frame or used with unit vector bases with transformations between the bird and inertial frames as needed.

By representing Eqn A3 in terms of the quantities listed above, we directly calculated the net aerodynamic torque about S_{CM}. A list of equations used during the derivation follows:

$$\frac{{}^{N}\mathrm{d}\,{}^{N}\vec{H}^{S/S_{\mathrm{CM}}}}{\mathrm{d}t} = \frac{{}^{N}\mathrm{d}\,{}^{N}\vec{H}^{\mathrm{T}/S_{\mathrm{CM}}}}{\mathrm{d}t} + \left(\sum_{i=1}^{n} \frac{{}^{N}\mathrm{d}\,{}^{N}\vec{H}^{P_i/S_{\mathrm{CM}}}}{\mathrm{d}t}\right), \tag{A4}$$

$${}^{N}\vec{H}^{P_i/S_{\mathrm{CM}}} = m^{P_i} * \vec{r}^{\,P_i/S_{\mathrm{CM}}} \times {}^{N}\vec{v}^{P_i}, \tag{A5}$$

$${}^{N}\vec{H}^{\mathrm{T}/S_{\mathrm{CM}}} = \underline{\boldsymbol{I}}^{\mathrm{T}/\mathrm{T}_{\mathrm{CM}}} \cdot {}^{N}\vec{\omega}^{\mathrm{T}} + m^{\mathrm{T}} * \vec{r}^{\,\mathrm{T}_{\mathrm{CM}}/S_{\mathrm{CM}}} \times {}^{N}\vec{v}^{\,\mathrm{T}_{\mathrm{CM}}}, \tag{A6}$$

$$\frac{{}^{N}\mathrm{d}\,{}^{N}\vec{H}^{P_i/S_{\mathrm{CM}}}}{\mathrm{d}t} = m^{P_i} * \left(\frac{{}^{N}\mathrm{d}\vec{r}^{\,P_i/S_{\mathrm{CM}}}}{\mathrm{d}t} \times {}^{N}\vec{v}^{P_i} + \vec{r}^{\,P_i/S_{\mathrm{CM}}} \times {}^{N}\vec{a}^{P_i}\right), \tag{A7}$$

$$\frac{{}^{N}\mathrm{d}\vec{r}^{\,P_i/S_{\mathrm{CM}}}}{\mathrm{d}t} = \frac{{}^{N}\mathrm{d}}{\mathrm{d}t}\vec{r}^{\,P_i/\mathrm{T}_{\mathrm{CM}}} - \frac{1}{m^{S}} * \left(\sum_{i=1}^{n}\left(m^{P_i} * \frac{{}^{N}\mathrm{d}}{\mathrm{d}t}\vec{r}^{\,P_i/\mathrm{T}_{\mathrm{CM}}}\right)\right), \tag{A8}$$

$$\frac{{}^{N}\mathrm{d}\vec{r}^{\,P_i/\mathrm{T}_{\mathrm{CM}}}}{\mathrm{d}t} = {}^{\mathrm{T}}\vec{v}^{P_i} + {}^{N}\vec{\omega}^{\mathrm{T}} \times \vec{r}^{\,P_i/\mathrm{T}_{\mathrm{CM}}}, \tag{A9}$$

$${}^{N}\vec{v}^{P_i} = \left(\left(-\frac{1}{m^{S}} * \left(\sum_{i=1}^{n}\left(m^{P_i} * \left({}^{\mathrm{T}}\vec{v}^{P_i} + {}^{N}\vec{\omega}^{\mathrm{T}} \times \vec{r}^{\,P_i/\mathrm{T}_{\mathrm{CM}}}\right)\right)\right) + {}^{N}\vec{\omega}^{\mathrm{T}} \times \vec{r}^{\,P_i/\mathrm{T}_{\mathrm{CM}}}\right) + {}^{\mathrm{T}}\vec{v}^{P_i}\right), \tag{A10}$$

The Journal of Experimental Biology (2015) doi:10.1242/jeb.104141

$$
{}^{N}\vec{a}^{P_i} = \Bigg(\Big(-\frac{1}{m^S} * \Bigg(\sum_{i=1}^{n} \Bigg(m^{P_i} * \Big(\Big({}^{T}\vec{a}^{P_i} + {}^{N}\vec{\omega}^{T} \times {}^{T}\vec{v}^{P_i} \Big) + \Big(\Big({}^{N}\vec{\alpha}^{T} \times \vec{r}^{\,P_i/T_{CM}} \Big) + \Big({}^{N}\vec{\omega}^{T} \times \Big({}^{T}\vec{v}^{P_i} + {}^{N}\vec{\omega}^{T} \times \vec{r}^{\,P_i/T_{CM}} \Big) \Big) \Big) \Big) \Bigg) \Bigg) + {}^{N}\vec{\alpha}^{T} \times \vec{r}^{\,P_i/T_{CM}} + {}^{N}\vec{\omega}^{T} \times \Big({}^{N}\vec{\omega}^{T} \times \vec{r}^{\,P_i/T_{CM}} \Big) \Bigg) + {}^{T}\vec{a}^{P_i} + 2\,{}^{N}\vec{\omega}^{T} \times {}^{T}\vec{v}^{P_i} \quad \text{(A11)}
$$

$$
\frac{{}^{N}\mathrm{d}\,{}^{N}\vec{H}^{T/S_{CM}}}{\mathrm{d}t} = \Big(\underline{\boldsymbol{I}}^{T/T_{CM}} \cdot {}^{N}\vec{\alpha}^{T} \Big) + \Big(m^{T} * \vec{r}^{\,T_{CM}/S_{CM}} \times {}^{N}\vec{a}^{T_{CM}} \Big), \quad \text{(A12)}
$$

$$
\vec{r}^{\,T_{CM}/S_{CM}} = \Bigg(-\frac{1}{m^S} * \Bigg(\sum_{i=1}^{n} m^{P_i} * \vec{r}^{\,P_i/T_{CM}} \Bigg) \Bigg), \quad \text{(A13)}
$$

$$
{}^{N}\vec{a}^{T_{CM}} = -\frac{1}{m^S} * \Bigg(\sum_{i=1}^{n} \Bigg(m^{P_i} * \Big(\Big({}^{T}\vec{a}^{P_i} + {}^{N}\vec{\omega}^{T} \times {}^{T}\vec{v}^{P_i} \Big) + \Big(\Big({}^{N}\vec{\alpha}^{T} \times \vec{r}^{\,P_i/T_{CM}} \Big) + \Big({}^{N}\vec{\omega}^{T} \times \Big({}^{T}\vec{v}^{P_i} + {}^{N}\vec{\omega}^{T} \times \vec{r}^{\,P_i/T_{CM}} \Big) \Big) \Big) \Big) \Bigg) \Bigg). \quad \text{(A14)}
$$

Finally, we arrived at:

$$
\begin{aligned}
\frac{{}^{N}\mathrm{d}\,{}^{N}\vec{H}^{S/S_{CM}}}{\mathrm{d}t} = \sum_{i=1}^{n} \Bigg(& m^{P_i} * \Bigg(\Bigg(\vec{r}^{\,P_i/T_{CM}} - \frac{1}{m^S} * \Bigg(\sum_{i=1}^{n} \Big(m^{P_i} * \vec{r}^{\,P_i/T_{CM}} \Big) \Bigg) \Bigg) \times \\
& \Bigg(-\frac{1}{m^S} * \Bigg(\sum_{i=1}^{n} \Bigg(m^{P_i} * \Big({}^{T}\vec{a}^{P_i} + {}^{N}\vec{\omega}^{T} \times {}^{T}\vec{v}^{P_i} + {}^{N}\vec{\alpha}^{T} \times \vec{r}^{\,P_i/T_{CM}} + {}^{N}\vec{\omega}^{T} \times \Big({}^{T}\vec{v}^{P_i} + {}^{N}\vec{\omega}^{T} \times \vec{r}^{\,P_i/T_{CM}} \Big) \Big) \Bigg) \Bigg) \\
& + {}^{N}\vec{\alpha}^{T} \times \vec{r}^{\,P_i/T_{CM}} + {}^{N}\vec{\omega}^{T} \times \Big({}^{N}\vec{\omega}^{T} \times \vec{r}^{\,P_i/T_{CM}} \Big) \\
& + {}^{T}\vec{a}^{P_i} + 2\,{}^{N}\vec{\omega}^{T} \times {}^{T}\vec{v}^{P_i} \Bigg) \Bigg) \Bigg) \\
& + \Big(\underline{\boldsymbol{I}}^{T/T_{CM}} \cdot {}^{N}\vec{\alpha}^{T} \Big) + m^{T} * \Bigg(-\frac{1}{m^S} * \Bigg(\sum_{i=1}^{n} \Big(m^{P_i} * \vec{r}^{\,P_i/T_{CM}} \Big) \Bigg) \Bigg) \times \Bigg(-\frac{1}{m^S} * \\
& \Bigg(\sum_{i=1}^{n} \Big(m^{P_i} * \Big({}^{T}\vec{a}^{P_i} + {}^{N}\vec{\omega}^{T} \times {}^{T}\vec{v}^{P_i} + {}^{N}\vec{\alpha}^{T} \times \vec{r}^{\,P_i/T_{CM}} \\
& + {}^{N}\vec{\omega}^{T} \times \Big({}^{T}\vec{v}^{P_i} + {}^{N}\vec{\omega}^{T} \times \vec{r}^{\,P_i/T_{CM}} \Big) \Big) \Big) \Bigg) \Bigg) \Bigg). \quad \text{(A15)}
\end{aligned}
$$

Eqn A15 simplified to Eqn 1.

Note that if there were no net aerodynamic torque about S_{CM}, ${}^{N}\vec{H}^{S/S_{CM}}$ would be constant, and any change in angular momentum of the wing-system would have to result in an opposite change in the angular momentum of the torso-system. Thus, by setting the right-hand side of Eqn A3 equal to zero for each time step and solving for ${}^{N}\vec{\alpha}^{T}$, we were able to calculate the angular acceleration of the torso and subsequent angular velocity and orientation changes that would have occurred if the pigeon had made the same movements in the absence of aerodynamic torque. The difference between the observed angular acceleration and predicted angular acceleration could be attributed to aerodynamic torque.

Acknowledgements

We thank P. A. Ramirez for care of the animals, D. E. Lieberman for kindly sharing the use of the Qualisys cameras, and A. N. Ahn, T. E. Higgins, J. J. Videler, E. J. Stamhuis, A. Eberle, C. Gastil, A. Randall and C. A. Moreno for helpful discussions and informal contributions to this work. We also thank two anonymous reviewers for improving the manuscript. This study was funded by grants from the National Science Foundation (NSF, IOS-0744056) and the Office of Naval Research (ONR, (N0014-10-1-0951) to A.A.B.

Competing interests

The authors declare no competing or financial interests.

Author contributions

I.G.R. and A.A.B. conceived, designed and executed the research. I.G.R., M.A.B. and A.N.P. analyzed the data. All authors interpreted the findings. I.G.R. drafted the article. I.G.R., A.A.B. and L.C.B. revised the article.

Funding

This research received no specific grant from any funding agency in the public, commercial, or not-for-profit sectors.

Supplementary material

Supplementary material available online at
http://jeb.biologists.org/lookup/suppl/doi:10.1242/jeb.104141/-/DC1

References

Aldridge, H. D. J. N. (1986). Kinematics and aerodynamics of the greater horseshoe bat, *Rhinolophus ferrumequinum*, in horizontal flight at various flight speeds. *J. Exp. Biol.* **126**, 479-497.
Alexander, R. M. (1968). *Animal Mechanics*. London: Sidgwick and Jackson.
Baier, D. B., Gatesy, S. M. and Dial, K. P. (2013). Three-dimensional, high-resolution skeletal kinematics of the avian wing and shoulder during ascending flapping flight and uphill flap-running. *PLoS ONE* **8**, e63982.
Bilo, D. (1994). Course control in flight. In *Perception and Motor Control in Birds* (ed. M. N. O. Davies and P. R. Green), pp. 227-247. Berlin: Springer-Verlag.
Bilo, D., Bilo, A., Muller, M., Theis, B. and Wedekind, F. (1985). Neurophysiological-cybernetic analysis of course control in the pigeon. In *Biona Report 3* (ed. W. Nachtigall), pp. 445-447. Stuttgart: Fischer.
Bilo, D. and Bilo, A. (1983). Neck flexion related activity of flight control muscles in the flow-stimulated pigeon. *J. Comp. Physiol.* **153**, 111-122.
Crandell, K. E. and Tobalske, B. W. (2011). Aerodynamics of tip-reversal upstroke in a revolving pigeon wing. *J. Exp. Biol.* **214**, 1867-1873.
Dial, K. P. (1992). Avian forelimb muscles and nonsteady flight: can birds fly without using the muscles in their wings? *Auk* **109**, 874-885.
Dial, K. P., Kaplan, S. R., Goslow, G. E., Jr and Jenkins, F. A., Jr (1988). A functional analysis of the primary upstroke and downstroke muscles in the domestic pigeon (*Columba livia*) during flight. *J. Exp. Biol.* **134**, 1-16.
Frohlich, C. (1980). The physics of somersaulting and twisting. *Sci. Am.* **242**, 154-165.
Hedrick, T. L. (2008). Software techniques for two- and three-dimensional kinematic measurements of biological and biomimetic systems. *Bioinspir. Biomim.* **3**, 034001.
Hedrick, T. L. and Biewener, A. A. (2007). Low speed maneuvering flight of the rose-breasted cockatoo (*Eolophus roseicapillus*). I. Kinematic and neuromuscular control of turning. *J. Exp. Biol.* **210**, 1897-1911.
Hedrick, T. L., Usherwood, J. R. and Biewener, A. A. (2007). Low speed maneuvering flight of the rose-breasted cockatoo (*Eolophus roseicapillus*). II. Inertial and aerodynamic reorientation. *J. Exp. Biol.* **210**, 1912-1924.
Hedrick, T. L., Cheng, B. and Deng, X. (2009). Wingbeat time and the scaling of passive rotational damping in flapping flight. *Science* **324**, 252-255.
Iriarte-Díaz, J. and Swartz, S. M. (2008). Kinematics of slow turn maneuvering in the fruit bat *Cynopterus brachyotis*. *J. Exp. Biol.* **211**, 3478-3489.
Iriarte-Díaz, J., Riskin, D. K., Willis, D. J., Breuer, K. S. and Swartz, S. M. (2011). Whole-body kinematics of a fruit bat reveal the influence of wing inertia on body accelerations. *J. Exp. Biol.* **214**, 1546-1553.

Mitiguy, P. (2014). *Dynamics of Mechanical, Aerospace, and Biomechanical Systems*. Sunnyvale, CA: Prodigy Press.
Newman, F. H. and Searle, V. H. L. (1957). *The General Properties of Matter*. London: Arnold.
Pratab, R. and Ruina, A. (2009). *Introduction to Statics and Dynamics*. Oxford: Oxford University Press.
Ros, I. G., Bassman, L. C., Badger, M. A., Pierson, A. N. and Biewener, A. A. (2011). Pigeons steer like helicopters and generate down- and upstroke lift during low speed turns. *Proc. Natl. Acad. Sci. USA* **108**, 19990-19995.
Su, J. Y., Ting, S. C., Chang, Y. H. and Yang, J. T. (2011). Aerodynamic trick for visual stabilization during downstroke in a hovering bird. *Phys. Rev. E Stat. Nonlin. Soft Matter Phys.* **84**, 012901.
van den Berg, C. and Rayner, J. M. V. (1995). The moment of inertia of bird wings and the inertial power requirement for flapping flight. *J. Exp. Biol.* **198**, 1655-1664.
Vazquez, R. J. (1995). Functional anatomy of the pigeon hand (*Columba livia*): a muscle stimulation study. *J. Morphol.* **226**, 33-45.
Walker, J. A. (1998). Estimating velocities and accelerations of animal locomotion: a simulation experiment comparing numerical differentiation algorithms. *J. Exp. Biol.* **201**, 981-995.
Warrick, D. R. (1998). The turning and linear maneuvering performance of birds: the cost of efficiency for coursing insectivores. *Can. J. Zool.* **76**, 1063-1079.
Warrick, D. R. and Dial, K. P. (1998). Kinematic, aerodynamic and anatomical mechanisms in the slow, maneuvering flight of pigeons. *J. Exp. Biol.* **201**, 655-672.
Warrick, D. R., Dial, K. P. and Biewener, A. A. (1998). Asymmetrical force production in the maneuvering flight of pigeons. *Auk* **115**, 916-928.
Winter, D. A. (2005). *Biomechanics and Motor Control of Human Movement*. Hoboken, NJ: Wiley.